

# Structural and Magnetic Properties of Ferrimagnetic $\epsilon$ -phase $\text{Mn}_4\text{N}$ and Antiferromagnetic $\zeta$ -phase $\text{Mn}_{10}\text{N}$ Thin Films on $\text{MgO}(001)$

Andrew Foley<sup>a</sup>, Joseph Corbett<sup>a</sup>, Andrea L. Richard<sup>a</sup>, Khan Alam<sup>a</sup>, David C. Ingram<sup>a</sup>, Arthur R. Smith<sup>a,\*</sup>

<sup>a</sup>*Nanoscale and Quantum Phenomena Institute, Department of Physics and Astronomy, Ohio University, Athens, OH 45701, USA*

---

## Abstract

Single phase  $\epsilon$ - $\text{Mn}_4\text{N}$  and  $\zeta$ - $\text{Mn}_{10}\text{N}$  thin films are grown on  $\text{MgO}(001)$  using molecular beam epitaxy. The films are identified and characterized using reflection high-energy electron diffraction, x-ray diffraction, back scattered electron scanning electron microscopy, atomic/magnetic force microscopy and Rutherford backscattering spectrometry. These films are found to be highly smooth with root-mean-squared roughnesses 3.39 nm and below. The quality of  $\epsilon$ - $\text{Mn}_4\text{N}$  grown is strongly dependent on substrate temperature during growth. Epitaxial growth of substantial grains composed of the antiferromagnetic  $\eta$ -phase  $\text{Mn}_3\text{N}_2$  side by side with ferrimagnetic  $\epsilon$ -phase grains is observed when growth temperature is below 480 °C. Ising domains isolated within areas roughly 0.5  $\mu\text{m}$  across are observed in the ferrimagnetic  $\epsilon$ -phase grains of samples consisting of a mix of  $\eta$ - and  $\epsilon$ -phase grains. Magnetic domains following semi-continuous paths, which are 0.7 to 7.2  $\mu\text{m}$  across, are observed in single phase  $\epsilon$ - $\text{Mn}_4\text{N}$ . Measurements of the  $\zeta$ -phase detail the structure and magnetism of the material as high Mn content  $\gamma$ -type  $\zeta$ -phase with a regular surface corrugation along the [100]-direction and antiferromagnetic.

*Keywords:* A1. Magnetic force microscopy, A3. Molecular beam epitaxy, B1. Nitrides, B2. Magnetic materials

*PACS:* 61.72.Mm, 68.55.J-, 75.70.Kw

---

---

\*Corresponding Author  
Email address: [smitha2@ohio.edu](mailto:smitha2@ohio.edu) (Arthur R. Smith)

## 1. Introduction

Transition metal (TM) nitrides such as  $(\text{Mn,Fe,Co})_x\text{N}_y$  have been demonstrated to possess a wide range of magnetic properties with tunability between different types of magnetism (e.g. ferromagnetic, antiferromagnetic, non-magnetic, ferrimagnetic) via phase control of each material.[1, 2, 3, 4] As well, at least one phase ( $\varepsilon\text{-Mn}_4\text{N}_1$ ,  $\alpha\text{-Fe}_x\text{N}_y$ ,  $\alpha''\text{-Fe}_{16}\text{N}_2$ , and  $\gamma\text{-Co}_3\text{N}_1$ ) of each of these three TM nitrides has shown perpendicular magnetic anisotropy (PMA) and consequently suitability for spin injection contacts.[5, 6, 7, 8] These two shared characteristics of tunable magnetic properties and suitability for spin injection contacts among these three TM nitrides suggest potential applications in giant magnetoresistance (GMR) devices.

$\text{Mn}_x\text{N}_y$  possesses three antiferromagnetic phases ( $\theta$ -,  $\eta$ - and  $\zeta$ -phase) and a single ferrimagnetic phase ( $\varepsilon$ -phase).[9] The  $\varepsilon$ -phase exhibits PMA with a highly polarizable *out-of-plane* easy axis alignment.[5] In agreement, theoretical calculations on  $\varepsilon\text{-Mn}_4\text{N}$  suggests the material has a high spin injection efficiency ( $>0.7$ ).[10]

In the past, reflection high-energy diffraction (RHEED) and X-ray diffraction (XRD) have served as the primary means for identifying the phase purity of  $\varepsilon\text{-Mn}_4\text{N}$  samples.[3, 5, 11, 12, 13, 14] However, phase impurities have been observed in epitaxially grown  $\varepsilon\text{-Mn}_4\text{N}$  when RHEED or XRD indicated otherwise.[3, 15] For this reason, an experiment determining the effect of growth temperature on phase purity of  $\varepsilon\text{-Mn}_4\text{N}$  grown on  $\text{MgO}(001)$  is of interest.

The antiferromagnetic  $\zeta$ -phase of  $\text{Mn}_x\text{N}_y$  is typically grown through incorporation of some gaseous form of N into solid Mn (e.g. reactive annealing).[9, 16, 17, 18] Additionally,  $\zeta$ -phase  $\text{Mn}_x\text{N}_y$  has been grown epitaxially on a hexagonal substrate (sapphire).[19] It has been proposed that the  $\zeta$ -phase does not grow on  $\text{MgO}(001)$  due to the hexagonal versus tetragonal nature of the  $\zeta$ -phase versus  $\text{MgO}$ . [3, 19] Unlike the other phases of  $\text{Mn}_x\text{N}_y$ , which each fall within a narrow range of Mn percentage (Mn%) values ( $\pm \sim 2\%$ ), the  $\zeta$ -phase has been found to be stable within a wide range from 64% to 92%.[9]

Starting with a growth study of  $\text{Mn}_4\text{N}$ , the growth is characterized using RHEED, XRD, Rutherford backscattering spectrometry (RBS) and AFM/MFM; and then the growth temperature is used to control the phase purity. Next, the application of these characterization techniques reveals the Mn% can be raised above the stability limit of  $\text{Mn}_4\text{N}$  ( $\sim 81.5\%$ ), which results in an upper stability limit  $\zeta$ -phase on  $\text{MgO}(001)$  ( $\sim 92\%$ ). This result represents the fourth and final phase of  $\text{Mn}_x\text{N}_y$  to be grown in a controlled manner on  $\text{MgO}(001)$ . [3, 17]

## 2. Procedure

All samples were prepared in a custom designed ultra-high vacuum molecular beam epitaxy system.[20] The  $\text{Mn}_x\text{N}_y$  samples were grown on  $\text{MgO}(001)$  substrates. Beforehand, the substrates were cleaned *ex situ* using solvent, first with acetone and then with isopropyl-alcohol. Additional *in situ* cleaning of the substrate was performed by annealing at a temperature of 1000 °C with

nitrogen plasma incident for  $\sim 1$  hr. Manganese flux was provided by a custom designed effusion cell operated at temperatures of  $\sim 1200$  °C, whereas N flux was supplied by an RF N Plasma Source (SVT Associates) with a forward power of 450 W and  $N_2$  as the source gas. The Mn flux is measured using a quartz crystal thickness monitor giving readings in  $\text{\AA}/s$ , while the effective N flux is determined by finding the crossover point between Ga- and N-rich GaN growth.[21] In total, twelve  $Mn_xN_y$  samples were grown using Mn fluxes in the range  $0.4-3 \times 10^{14}$  Mn atoms/( $\text{cm}^2s$ ) and effective N fluxes in the range of  $0.5-1.4 \times 10^{14}$  atoms/( $\text{cm}^2s$ ). On occasion, to induce the  $\zeta$ -phase (highest Mn content) growth, the N source shutter was adjusted to interrupt the N flux.

RHEED is actively used *in situ* during growth with a 20 keV incident electron beam energy in order to monitor the phase of growth based on the observation of phase specific surface structure/reconstruction; this is determined by measuring, for example, the characteristic RHEED streak spacings and from these determining the *in-plane* lattice constant(s) by means of the RHEED calibration. The calibration is performed for each growth using the MgO substrate post-annealing streak spacings as a reference. XRD is applied *ex situ* employing  $Cu K_\alpha$  x-rays in order to determine the bulk crystal structure normal to the substrate surface including atomic spacings prevalent in the samples. The bulk Mn:N ratios in the samples are determined using RBS. Relative Mn concentration between different crystal grains is determined using back scattered electron scanning electron microscopy (BSE-SEM). Atomic/magnetic force microscopy is performed using a Park Scientific CP AFM/MFM head retrofitted with a controller system by Anfatec Inc. which is operated *ex situ* to obtain information about the samples' topographical and magnetic properties. The MFM is performed in phase contrast mode, giving a picture of the samples' stray field map at a certain height  $z$  above the sample plane. Analysis of the obtained stray field maps is used to infer sample domain structure.

### 3. Growth Summary

Variation of the sample growth parameters in this study enabled the synthesis of qualitatively three different types of  $Mn_xN_y$  phases including two approximately pure phase samples ( $\varepsilon$  and  $\zeta$ ) and one mixed-phase sample ( $\eta + \varepsilon$ ). Although growth of  $\eta$ -phase is typically achieved at sample temperatures up to 450 °C, and the growth of  $\varepsilon$ -phase can be achieved at sample temperatures above 450 °C, growth of  $\zeta$ -phase favors not only temperatures of  $\sim 480$  °C or higher but also requires a growth interrupt to trigger this less common phase to appear; this could be achieved either by temporarily closing the plasma shutter to interrupt N-flux during growth, or a post-growth annealing step.

Figure 1(a) shows the RHEED pattern characteristic of all of the post-annealing MgO substrates on which each of the three samples were grown. The bright uniform streaks together with the sharp Kikuchi lines within the characteristic RHEED pattern of these substrates shows that the substrate surface was highly-smooth, well-ordered MgO suitable for RHEED calibration. Figures 1(b-d) and 2 present the RHEED and XRD patterns, respectively, for the

three types of samples to be focused on in this study with all associated values tabulated in Table 1. The presentation begins with a discussion of the diffraction (RHEED, XRD) data for the lower growth temperature ( $\eta + \varepsilon$ ) mixed phase (sample A), the middle growth temperature ( $\varepsilon$ ) sample (sample B) and then, after introducing the RBS data, the higher growth temperature ( $\zeta$ ) sample (sample C).

The presentation finishes with a discussion of the microscopy data (AFM, MFM, BSE-SEM) of samples A, B and then C. The requirement of a substrate temperature over 450 °C for growth of samples B ( $\varepsilon$ -phase) and C ( $\zeta$ -phase) is consistent with Yang *et al.*, in which at 450 °C the growth of high purity  $\varepsilon$ -phase or any  $\zeta$ -phase was unobserved.[3] Samples in this study were not intentionally annealed for any significant times, although it has been shown that  $\theta$ ,  $\eta$ ,  $\zeta$ , and  $\varepsilon$  (up to as high as 4:1 Mn:N) can be achieved by successively increasing annealing temperatures which results in increasing levels of N loss.[16]

#### 4. Crystallography

The RHEED and XRD taken from the 450 °C sample (sample A) are shown in Fig. 1(b) and Fig. 2(a) respectively. Figure 1(b) shows 1st order streaks and faintly visible half-order streaks, with the 1st order streak spacing corresponding to an  $a$ -spacing of  $3.97 \pm 0.02$  Å in the lattice. This value agrees well with an average (3.99 Å) between values for  $\varepsilon$ -phase (3.86 Å) and  $\eta$ -phase (4.04/4.21 Å), thus indicating a mixture of  $\eta$ - and  $\varepsilon$ -phases.[9] As well, the faint half-order streaks indicate a partial occupation of  $\varepsilon$ -phase at the surface of sample A. It should be noted that the same  $a$ -spacing was reported by Yang *et al.* for a sample reported as  $\varepsilon$ -phase with some  $\eta$ -phase impurity.[3] As shown in Fig. 2(a), XRD finds 5 significant peaks within the  $2\theta$  range of 35–50 degrees, including a substantial  $\varepsilon$ -phase 002 peak occurring at  $2\theta = 47.00$  deg, a very small  $\zeta$ -phase 101 peak, a barely visible  $\zeta$ -phase 002 peak, a large MgO 002 peak (split peak due to saturation of the detector), and a small intensity MgO 111 peak (coming from the back-side of the substrate). The  $\varepsilon$ -phase 002 peak is slightly shifted compared to the expected, giving a  $3.87 \pm 0.01$  Å  $c$ -spacing, while the  $\eta$ -phase  $\text{Mn}_3\text{N}_2$  020 peak is indistinguishable from the MgO 002 peak. A perspective view of the  $\eta$ - $\text{Mn}_3\text{N}_2$  and  $\varepsilon$ - $\text{Mn}_4\text{N}$  structures can be seen, in which (010) and (001) Mn planes are indicated, in Fig. 3(a-b) respectively.

A substrate temperature of 480°C was used to grow the  $\varepsilon$ - $\text{Mn}_4\text{N}$  sample (sample B); with the [100] surface reconstruction demonstrated by RHEED and the bulk composition determined from XRD. First order [100] RHEED streak spacings are measured in Fig. 1(c), resulting in a deduced (after calibration)  $3.88 \pm 0.01$  Å  $a$ -spacing. Clearly visible half-order streaks agree with the accepted structure (4 Mn in fcc structure with a single N at the body center) by showing a  $2 \times$  periodicity perpendicular to the [100]-direction.[22] This  $2 \times$  periodicity is due to the non-degeneracy between face-centered and corner Mn atoms doubling the distance between degenerate Mn atoms along this direction. The appearance of faint Kikuchi lines suggests a high quality, flat, and well-ordered  $\varepsilon$ -phase surface. The XRD pattern for sample B shown in Fig. 2(b) contains the same

set of XRD peaks as for sample A, but with strongly increased  $\varepsilon$ -phase 002 peak intensity and a significant reduction in the  $\zeta$ -phase peaks. From the  $\varepsilon$ -phase peak position, a  $c$ -spacing of  $3.86 \pm 0.01$  Å is determined. The 3.88 Å  $a$ -spacing and 3.86 Å  $c$ -spacing, as determined by RHEED and XRD respectively, both agree well with the expected value for  $\varepsilon$ -phase (3.86 Å).[9]

The RHEED and XRD taken from the 510 °C sample (sample C) are shown in Fig. 1(d) and Fig. 2(c), respectively. The RHEED pattern shown in Fig. 1(d) shows split 1st and 2nd order streaks, which together indicate two *in-plane* spacings of  $4.95 \pm 0.10$  Å (bottom arrow dotted) and  $5.23 \pm 0.15$  Å (bottom arrow solid). There is also a streak (bottom arrow dotted) with an associated spacing of  $9.87 \pm 0.22$  Å, which is close to  $2 \times$  the 4.95 Å spacing. As well, there is a 1st order streak (top arrow) showing a  $3.80 \pm 0.24$  Å *in-plane* spacing with a chevron, which is observed in the angular splitting at the bottom of the streak. Such chevron features can be characteristic of refraction effects due to surface faceting.[26] However, the observed chevrons are too weak and apex location too unclear to obtain an accurate measurement of the angle between the facet and the growth plane.

X-ray diffraction in Fig. 2(c) shows no 002  $\varepsilon$ -phase peak, but instead a sizeable 101  $\zeta$ -phase peak corresponding to a  $d$ -spacing of 2.15 Å, and two additional  $\zeta$ -phase peaks (002 and 100), corresponding to  $d$ -spacings of 4.53 Å (002) and 2.43 Å (100). These measured  $d$ -spacings agree with known values for  $\gamma$ -type  $\zeta$ -phase  $Mn_xN_y$  presented by Leineweber *et al.* and are shown in Table 1.[17] Corresponding to the three  $\zeta$ -phase peaks seen in the XRD are three planes within the perspective view of the  $\gamma$ -type  $\zeta$ -phase model shown in Fig. 3(c). The 002 XRD peak corresponds to the interplanar distance between  $c$ -planes in the  $\gamma$ -type  $\zeta$ -phase structure with known  $c$ -spacing 4.55 Å. The 101 XRD peak corresponds to (101) planes of the zeta structure which have known interplanar spacings of 2.15 Å. Finally, the 100 XRD peak corresponds to (100) zeta structure planes which have interplanar spacings of  $2.83$  Å  $\times$   $\cosine(30^\circ) = 2.45$  Å. Based on these agreements between measured XRD spacings and known  $\zeta$ -phase interplanar spacings, we conclude that there are at least three different orientations of  $\zeta$ -phase grains within the film.

The measured RHEED pattern spacings can be seen to correspond to *in-plane* spacings of the three  $\zeta$ -phase grain orientations found from XRD. Corresponding to (001)  $c$ -planes, the long diagonal along  $[1\bar{1}0]$  is  $2.83$  Å  $\times$   $\sqrt{3} = 4.91$  Å, agreeing well with the RHEED spacing of  $4.95 \pm 0.1$  Å. Corresponding to the (101) planes, the atomic spacing along the  $[10\bar{1}]$  direction is  $\sqrt{(2.83 \text{ Å})^2 + (4.55 \text{ Å})^2} = 5.36$  Å which is within error of the measured RHEED spacing of  $5.23 \pm 0.15$  Å. Corresponding to the (100)  $a$ -planes, the relevant atomic spacing along the  $[011]$  direction is  $\sqrt{(2.83 \text{ Å})^2 + (4.55 \text{ Å})^2} = 5.36$  Å which also agrees with the measured RHEED spacing  $5.23 \pm 0.15$  Å within error. Finally, if we assume (304) facets, which are slightly off of (101) planes, we get an inter-atomic spacing of 3.99 Å along  $[\frac{2}{3} \frac{2}{3} \frac{1}{2}]$ , which is in reasonable agreement with the measured  $3.80 \pm 0.24$  Å spacing seen in RHEED. In total, all the RHEED and XRD spac-

ing measurements are consistent with a film having (101), (001), and (100) orientations of the  $\zeta$ -phase structure with possible (304) oriented facet planes.

Further evidence for the  $\gamma$ -type  $\zeta$ -phase identification of sample C is obtained by measuring stoichiometry with RBS. A wide range of potential stoichiometries are associated with the  $\zeta$ -phase.[9, 17] RBS taken on the  $\zeta$ -phase samples grown on MgO(001) in this experiment indicates an approximately 10:1 Mn:N ratio (90.9% Mn). This 90.9% Mn concentration approaches the highest Mn% observed for the  $\zeta$ -phase (92%), which suggests either  $\varepsilon$ -type (hexagonal with ordered N-site occupation) or  $\gamma$ -type (hexagonal with disordered N-site occupation)  $\zeta$ -phase, the two most Mn-rich types, was grown.[9, 17]

The  $\varepsilon$ -type  $\zeta$ -phase unit cell contains 8 Mn and 6 N-sites.[17] This means a 10:1 Mn:N ratio would require a unit cell to have less than one N-atom on average (0.8). Therefore, the size of the  $\varepsilon$ -type  $\zeta$ -phase unit cell is too small to contain well-ordered N-site occupation at this Mn:N ratio. It follows that a 10:1 Mn:N ratio indicates primarily disordered N-vacancies, which identifies the majority of the 510 °C sample (sample C) as  $\gamma$ -type  $\zeta$ -phase.

The model in Fig. 3(c) shows the N-sites fully occupied. Randomly-incorporated N-vacancies can be added to the model until the stability limit is reached.[9, 17] This can allow agreement with the measured 90.9% Mn concentration. Clearly, growth of hexagonal  $\zeta$ -phase  $\text{Mn}_x\text{N}_y$  on a tetragonal MgO (001)-oriented substrate is favored at high Mn concentrations such as that shown here.

## 5. Morphology and Magnetism

AFM, MFM and (BSE-SEM) images from a mixed phase sample (sample A) are shown in Figs. 4 and 5. These results reveal the growth of a smooth surface consisting of a mix of mostly  $\varepsilon$ - and  $\eta$ -phase domains. Two distinct morphologies, a smaller and larger cross-hatching, are seen in the AFM image in Figs. 4(a). These cross-hatchings consists of islands overlapping and elongated along the two degenerate [110] directions, which is consistent with the cubic structure of the material. A cross-section through the center of the ring-shaped Fast Fourier Transform (FFT) consists of a double peak, and the average of the two widths at 1/e of the maxima provides the range of distances typically found along a particular direction within an image.[23] This analysis is performed on the small and large cross-hatching to determine a range of the width and length of the islands in each. The range of the width and length of the islands found in the small cross-hatching are 0.6 to 1.0  $\mu\text{m}$  and 0.4 to 7.5  $\mu\text{m}$  respectively. The range of the width and length of the islands found in the large cross-hatching are 0.3 to 1.8  $\mu\text{m}$  and 1.8 to 13.3  $\mu\text{m}$  respectively. Unlike the cross-hatching, the edges of the grains follow irregular paths without any particular alignment(s).

The MFM image in Fig. 4(b) shows the magnetic contrast corresponding to the area shown in Fig. 4(a). The solid and dotted line profiles, showing topographic and magnetic signals respectively, in Fig. 4(c) indicate that the two different types of cross-hatched morphologies correspond to regions having different magnetic properties. From the magnetic line profile (dotted) the magnetic domains are roughly half a micrometer across. In agreement, an FFT

analysis of sample A following the procedure of Bai *et al.* gives a range of magnetic domain widths of 0.25 to 1.62  $\mu\text{m}$ . [23] The up-to-1.62  $\mu\text{m}$  wide domains are therefore having a flat 2D-like shape given the film thickness of 0.2  $\mu\text{m}$ .

The magnetic domains in the larger cross-hatched morphology of sample A are identified as "pancakelike" Ising domains by the associated magnetic domain structure (isolated and flattened). [24] The magnetic domains appear to be partially aligned with the same two degenerate [110] directions as the two cross-hatching morphologies. Conversely, the areas having smaller cross-hatched morphology do not reveal any observable magnetic contrast.

The presence of magnetic domains identifies the larger cross-hatching as either ferrimagnetic or ferromagnetic. Meanwhile, the indiscernible magnetic contrast identifies the smaller cross-hatching as either antiferromagnetic or non-magnetic. Ferrimagnetism and antiferromagnetism are the only two types of magnetism found in the  $\text{Mn}_x\text{N}_y$  system. [9] Therefore, the larger and smaller cross-hatched regions are identified as being ferrimagnetic and antiferromagnetic respectively. The ferrimagnetic domains are readily identified as  $\epsilon$ - $\text{Mn}_4\text{N}$  because this is the only ferrimagnetic phase of  $\text{Mn}_x\text{N}_y$  and there is a sufficiently large  $\epsilon$ -phase 002 XRD peak to explain the fraction of the surface containing ferrimagnetic domains (roughly half).

Larger AFM images such as Fig. 5(a) find that the antiferromagnetic grains are consistently raised above the ferrimagnetic domains. An example of this height difference is shown in the line profile in Fig. 4(c), in which there is a rise of roughly 5 nm during the transition from ferrimagnetic to antiferromagnetic areas. These raised antiferromagnetic areas are identified to be Mn-poor compared to the lower lying grains using BSE-SEM as seen in Fig. 5(b), in which a heat mapping of Mn concentration is laid over the 3-D topography of a 190  $\mu\text{m}$  area.

Due to the raised grains being observed with AFM/MFM in an abundance covering roughly half the surface, a corresponding XRD peak would be expected to occur with a number of counts of the same order of magnitude as the  $\epsilon$ -phase 002 peak. However, the only peaks in Fig. 2(a) aside from the  $\epsilon$ -phase peak are two  $\zeta$ -phase peaks, which even together are too small to explain the raised grains with lower Mn concentrations occupying roughly half the surface. Therefore, we can identify the raised grains as having  $\eta$ - $\text{Mn}_3\text{N}_2$  (010) structure because this is the only known  $\text{Mn}_x\text{N}_y$  structure with a peak that would be completely obscured by another, specifically the MgO 002 peak. Additionally, the observations that the raised grains are antiferromagnetic and have a lower Mn concentration agree with an  $\eta$ -phase identification of the antiferromagnetic grains. Furthermore, this is consistent with the RHEED data from Fig. 1(b), including a diminished half-order streak intensity and a 1st order spacing the average of eta- and epsilon-phase spacings, supporting a mix of  $\eta$ - and  $\epsilon$ -phase grains for this sample.

Roughness analysis of the 30  $\mu\text{m}$  image in Fig. 5(a) indicates an RMS roughness of 3.39 nm with a height range of 19.8 nm across the surface. The origin of the roughness comes mainly from the height difference between eta- and epsilon-phase regions. The relatively low RMS roughness and height range are favorable

values for potentially patterning a mix of antiferromagnetic and ferrimagnetic domains on a surface. It should be noted, there are two morphologies, cross-hatched and disordered (circled), observed within the  $\eta$ -phase regions in Fig. 5(a) compared to the single morphology seen within the  $\varepsilon$ -phase regions. This lack of morphological uniformity is likely explained by the Mn-rich growth conditions, which are not ideal for  $\eta$ -phase growth (Mn:N ratio significantly greater than the 0.87 identified by Yang *et al.*).[3] Despite the non-ideal conditions,  $\eta$ -phase grain growth persists for hundreds of nanometers. This fact indicates that controlling the growth conditions during the initial growth stage of nucleation is important for  $\text{Mn}_x\text{N}_y$  growth because a mix of grains will propagate through the entire film, even if growth conditions are non-ideal for some or all of the grains.

AFM/MFM results for an  $\varepsilon$ -phase sample (sample B) are shown in Fig. 6, which presents the growth of a highly smooth surface. The  $20\ \mu\text{m}$  AFM image shown in Fig. 6(a) demonstrates an RMS roughness of 0.33 nm with a height range of 1.52 nm. The morphology of the  $\varepsilon$ -phase sample (sample B) can be seen more clearly in Fig. 6(c). This morphology consists of exceptionally flat square-shaped terraces (generally between 0.1 to 0.5  $\mu\text{m}$  in width). The line profile (solid) in Fig. 6(d) further illustrates a highly smooth surface with a small height variation, less than 1.5 nm.

The MFM image corresponding to Fig. 6(a) is shown in Fig. 6(b), which demonstrates the magnetic domains characteristic of sample B. The sample B magnetic domains do not show any crystalline alignment. It is evident from the magnetic line profile (dotted) in Fig. 6(d) that the sample B magnetic domains are from roughly 0.5 to 5  $\mu\text{m}$  across. In agreement, an FFT analysis of sample B following the procedure of Bai *et al.* gives a range of magnetic domain widths of 0.7 to 7.2  $\mu\text{m}$ . [23] The up-to-7.2  $\mu\text{m}$  wide magnetic domains are relatively 2-dimensional given the only 0.1  $\mu\text{m}$  thick film. Many of the magnetic domains are laid out in paths, which are continuous across the entire image shown in Fig. 6(b).

The sample B magnetic domain shape (0.7 to 7.2  $\mu\text{m}$  across and laid out in semi-continuous paths) is in contrast to the sample A magnetic domain shape (roughly half a micrometer across and isolated). There are multiple potential causes for the  $\varepsilon$ -phase in sample A having smaller magnetic domains than sample B, including the following: the smaller  $\varepsilon$ -phase grain size and/or strain induced by the adjacent  $\eta$ -phase grains affecting the domain size.[14, 25] Additionally, the RMS roughness and height range of sample B (0.33 and 1.52 nm respectively) are both an order of magnitude below those of sample A (3.39 and 19.8 nm respectively). Clearly, an  $\varepsilon$ -phase sample with greatly enhanced crystal phase purity can be grown when the substrate growth temperature is raised to 480  $^\circ\text{C}$ .

AFM/MFM results from a  $\zeta$ -phase sample are shown in Fig. 7, in which a stripe-like pattern with stripes running parallel to  $100_{MgO}$  is observed. Line section measurements across the stripe-like pattern, as shown in Fig. 7(d), indicate a typical corrugation width and height of  $\sim 70\text{--}90$  nm and  $\sim 1\text{--}3$  nm, respectively. The observation of corrugation dimensions being semi-periodic

suggests that the surface is faceted and may agree with the observation of weak chevrons seen in the RHEED pattern in Fig. 1(d). The AFM measured width and height correspond to a slope of  $\arctangent(\frac{1}{45} \frac{nm}{nm}) = 1.27^\circ$  to  $\arctangent(\frac{3}{35} \frac{nm}{nm}) = 4.90^\circ$  with respect to the growth plane, which is below the  $7.79^\circ$  separation between the (304)- and (101)-planes. This angular difference suggests that the slope is a mixture of (304) and (101) facets, which agrees with the observation of both 3.80 Å and 5.23 Å spacings in RHEED.

No grain boundaries were observed in the AFM images of the  $\zeta$ -phase sample despite RHEED and XRD results both indicating the sample contains a mix of grains. This discrepancy may be explained by the scale of the grain size being too large to observe grain boundaries with this AFM. Occasionally, some macrosteps having heights of  $\sim 2-3$  nm and running perpendicular to  $100_{MgO}$ , as seen in Fig. 7(a), are also observed. Roughness analysis of Fig. 7(a) gives an RMS roughness of 0.84 nm and a height range of 4.62 nm across the  $2 \mu m$  sized image. The sample is therefore highly smooth while at the same time faceted.

The MFM image in Fig. 7(b) shows the localized stray field of the  $\zeta$ -phase sample over the area observed in Fig. 7(a). Contrast features of the MFM image match quite closely the features in the AFM image. This comparison suggests that the magnetic image contains no magnetic stray field signal with only the remnant topographic signal coming through.[27] As seen in comparing the topographic (dotted) and magnetic (solid) line profiles in Fig. 7(d) the MFM signal does not exactly match the height variation. However, the agreement is good enough that we exclude the presence of stray field in the sample. This measurement is consistent with the  $\zeta$ -phase sample being antiferromagnetic.

## 6. Conclusions

In conclusion, beyond the Mn:N flux ratio, a high dependence on substrate growth temperature is reported. Increasing the growth temperature from 450 to 480 °C results in single phase  $\varepsilon$ -Mn<sub>4</sub>N growth without the significant incorporation of  $\eta$ -phase grains as found in 450 °C growths. Growth of  $\varepsilon$ - and  $\eta$ -phase grains side by side indicates that the control of growth parameters during initial nucleation is especially important. Side by side growth of  $\varepsilon$ - and  $\eta$ -phases is of interest as a method for the organization of magnetic properties within a sample. However, a method for controlling the nucleation sites of  $\varepsilon$ - and  $\eta$ -phases would still need to be determined in order to controllably pattern the magnetism. The vertical direction of this side by side growth indicates the Mn<sub>x</sub>N<sub>y</sub> has greater suitability for lateral organization compared to vertical layering.

As well, with an increased growth temperature (510 °C) and when deprived sufficiently of N, upper Mn:N ratio stability limit hexagonal  $\gamma$ -type  $\zeta$ -phase can be grown epitaxially on a tetragonal MgO(001) substrate with a stripe-like superstructure. Although a dominant (101) growth orientation can be achieved, the feasibility of epitaxial growth of single grain  $\zeta$ -phase on MgO(001) remains uncertain.

## 7. Acknowledgements

Research has been supported by the U.S. Department of Energy, Office of Basic Energy Sciences, Division of Materials Sciences and Engineering under Award # DE-FG02-06ER46317. A. Foley wishes to thank Andrada-Oana Mandru for useful discussion and Martin Kordesch for the back-coating of substrates as well as useful discussion. Additionally, A.F. wishes to thank Doug Shafer and Mike Myers for machining many of the system components and their help maintaining the system. The authors acknowledge the WSxM software for image processing.[28]

- [1] M. Matsuoka, K. Ono, T. Inukai, *Appl. Phys. Lett.* **49**, 977 (1986).
- [2] M. Gupta, A. Gupta, S. M. Chaudhari, D. M. Phase, V. Ganesan, M. V. Rama Rao, T. Shripathi, B. A. Dasannacharya, *Vacuum* **60**, 395 (2001).
- [3] H. Yang, H. Al-Britthen, E. Trifan, D. Ingram, A. R. Smith, *J. Appl. Phys.* **91**, 1053 (2002).
- [4] M. B. Lourenço, M. D. Carvalho, P. Fonseca, T. Gasche, G. Evans, M. Godinho, M. M. Cruz, *J. Alloys Compd.* **612**, 176 (2014).
- [5] K. M. Ching, W. D. Chang, T. S. Chin, J. G. Duh, H. C. Ku, *J. Appl. Phys.* **76**, 6582 (1994).
- [6] A. Gupta, R. Dubey, W. Leitenberger, U. Pietsch, *Appl. Phys. Lett.* **92**, 052504 (2008).
- [7] N. Ji, M. S. Osofsky, V. Lauter, L. F. Allard, X. Li, K. L. Jensen, H. Ambaye, E. Lara-Curzio, J.-P. Wang, *Phys. Rev. B* **84**, 245310 (2011).
- [8] M. Matsuoka, K. Ono, T. Inukai, *IEEE T. Magn.* **23**, 2788 (1987).
- [9] N. A. Gokcen, *Bull. Alloy Phase Diagr.* **11**, 33 (1990).
- [10] M. S. Miao, A. Herwadkar, W. R. L. Lambrecht, *Phys. Rev. B* **72**, 033204 (2005).
- [11] S. Dhar, O. Brandt, K. H. Ploog, *Appl. Phys. Lett.* **86**, 112504 (2005)
- [12] D. Vempaire, D. Fruchart, R. Gouttebarron, E. K. Hill, S. Miraglia, L. Ortega, J. Pelletier, *Physica A. Stat. Mech. and its Appl.* **358**, 136 (2005).
- [13] C. Li, Y. Yang, L. Lv, H. Huang, Z. Wang, S. Yang, *J. Alloys Compd.* **457**, 57-60 (2008).
- [14] Y. Yasutomi, K. Ito, T. Sanai, K. Toko, T. Suemasu, *J. Appl. Phys.* **115**, 17A935 (2014).
- [15] X. Shen, A. Chikamatsu, K. Shigematsu, Y. Hirose, T. Fukumura, T. Hasegawa, *Appl. Phys. Lett.* **105**, 072410 (2014).

- [16] K. Suzuki, T. Kaneko, H. Yoshida, Y. Obi, H. Fujimora, H. Morita, J. Alloys Compd. **306**, 66-71 (2000).
- [17] A. Leineweber, H. Jacobs, W. Kockelmann, J. Alloys Compd. **368**, 229 (2004).
- [18] Z. Sun, X. Song, Mat. Lett. **63**, 2059 (2009).
- [19] Y. Liu, L. Xu, X. Li, P. Hu, S. Li, J. Appl. Phys. **107**, 103914 (2010).
- [20] W. Lin, A. Foley, K. Alam, K. Wang, Y. Liu, T. Chen, J. Pak, and A. R. Smith, Rev. Sci. Instrum. **85**, 043702 (2014).
- [21] K. Alam, A. Foley, A. R. Smith, Nano Lett. **15**, 2079-2085 (2015).
- [22] W. J. Takei, R. R. Heikes, G. Shirane, Phys. Rev., **125**, 1893 (1962)
- [23] F. Bai, J. Li, D. Viehland, D. Wu, T. A. Lograsso, J. Appl. Phys. **98** 023904 (2005).
- [24] W. Wu, V. Kiryukhin, H.-J. Noh, K.-T. Ko, J.-H. Park, W. Ratcliff II, P. A. Sharma, N. Harrison, Y. J. Choi, Y. Horibe, S. Lee, H. T. Yi, C. L. Zhang, S.-W. Cheong, Phys. Rev. Lett. **101**, 137203 (2008).
- [25] K. M. Ching, W.D. Chang, T. S. Chin, Appl. Surf. Sci. **92**, 471-471 (1996).
- [26] G. J. Whaley, P. I. Cohen, MRS Proceedings **160**, 35 (1989).
- [27] S. Porthun, L. Abelmann, C. Lodder, J. Magn. Magn. Mater. **182**, 238 (1998).
- [28] I. Horcas, R. Fernandez, J. M. Gomez-Rodriguez, J. Colchero, J. Gomez-Herrero and A. M. Baro, Rev. Sci. Instrum. **78**, 013705 (2007).

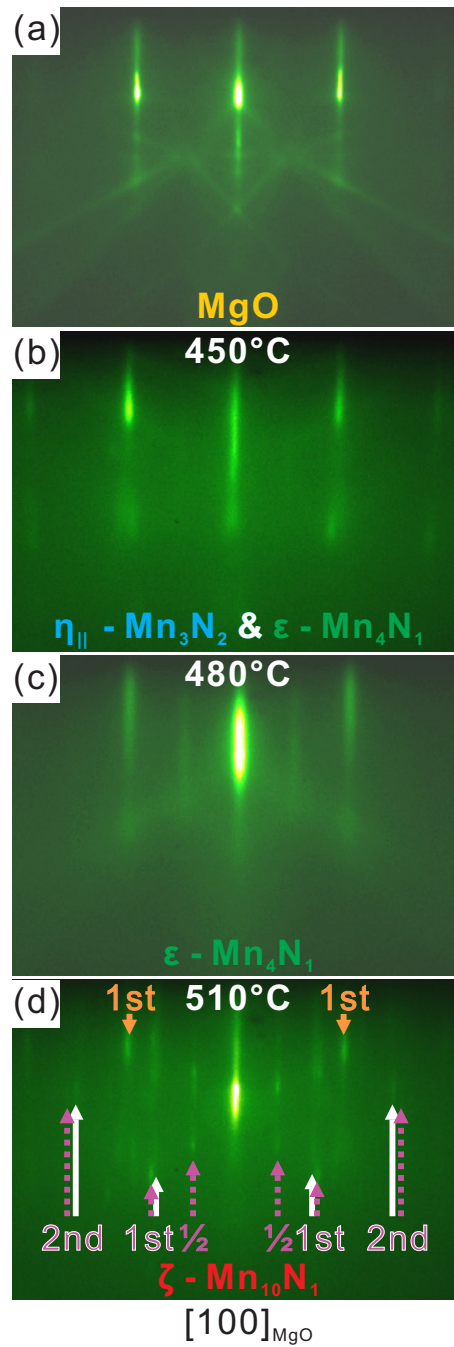


Figure 1: RHEED images taken along the MgO[100] direction of the three types of samples grown as well as a bare MgO substrate. The images correspond to the samples as follows (a) Bare MgO substrate (b) Mix of  $\eta_{||}$ -phase and  $\varepsilon$ -phase (c)  $\varepsilon$ -phase (d)  $\zeta$ -phase

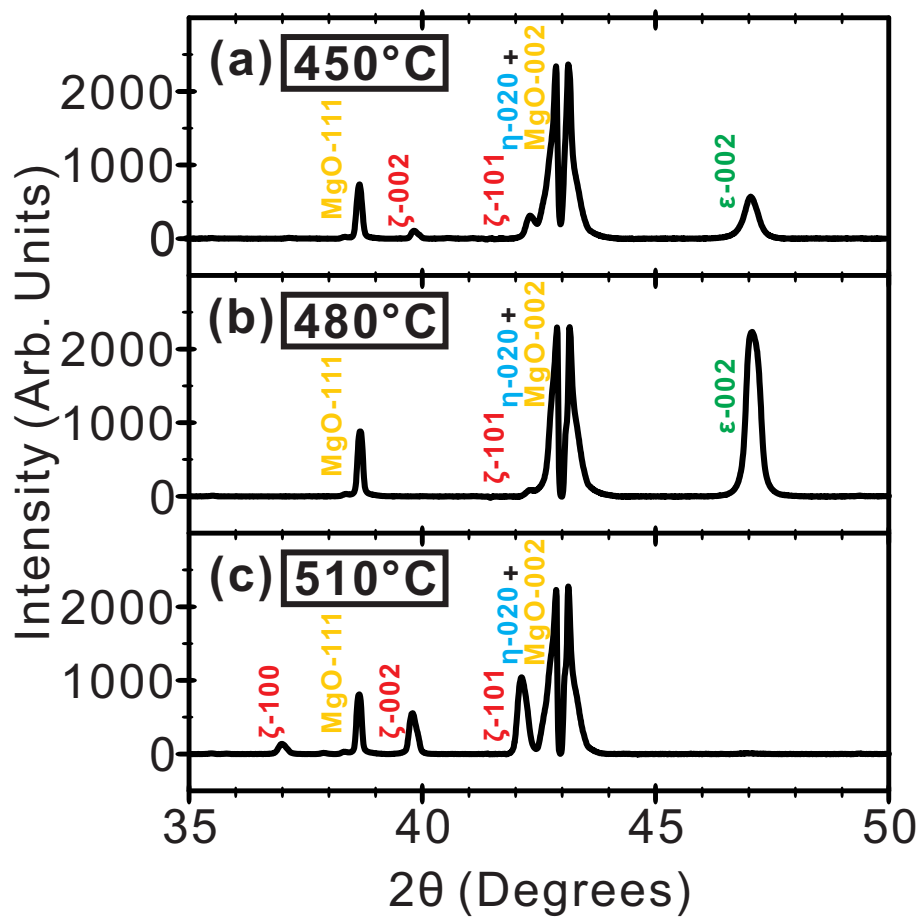


Figure 2: (a)-(c) XRD of the three types of samples grown. The images correspond to the samples as follows (a) Mix of  $\eta_{||}$ -phase and  $\epsilon$ -phase (b)  $\epsilon$ -phase (c)  $\zeta$ -phase.

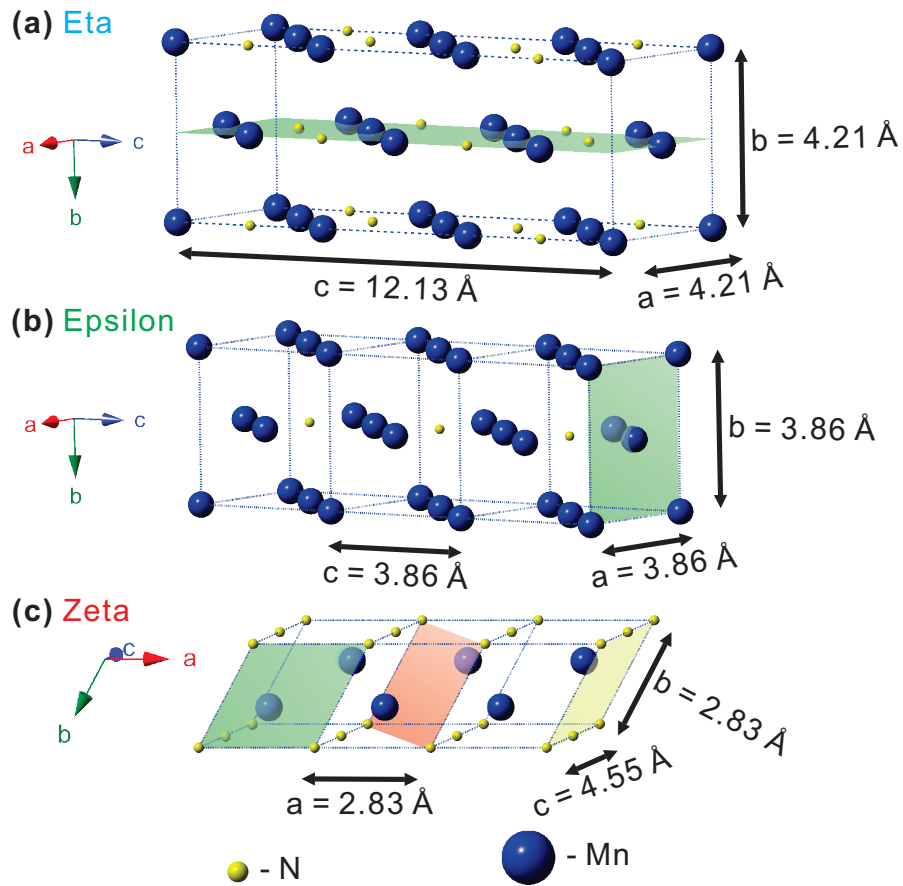


Figure 3: (a)-(c) Models corresponding to values found in literature of each of the three phases grown shown in perspective view.[3, 17] The images correspond to the phases as follows (a)  $\eta_{||}$ -phase with a (020) Mn-plane (b)  $\epsilon$ -phase with a (002) Mn-plane (c)  $\gamma$ -type  $\zeta$ -phase with (002), (101), and (100) Mn-planes (left, middle and right respectively).

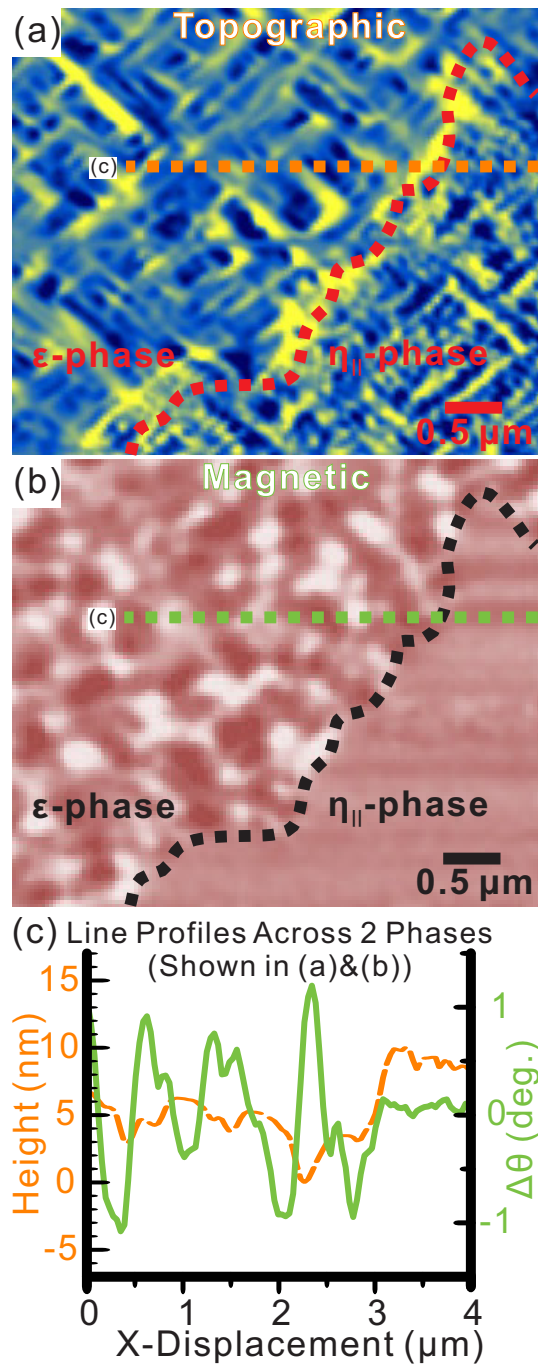


Figure 4: Microscopy data of the mixed phase sample. (a) AFM image showing the domain boundary between an  $\epsilon$ -phase domain left and an  $\eta_{||}$ -phase domain right (b) MFM image of the same area shown in a) (c) Topographic solid line profile and magnetic dotted line profile seen in a) and b) respectively

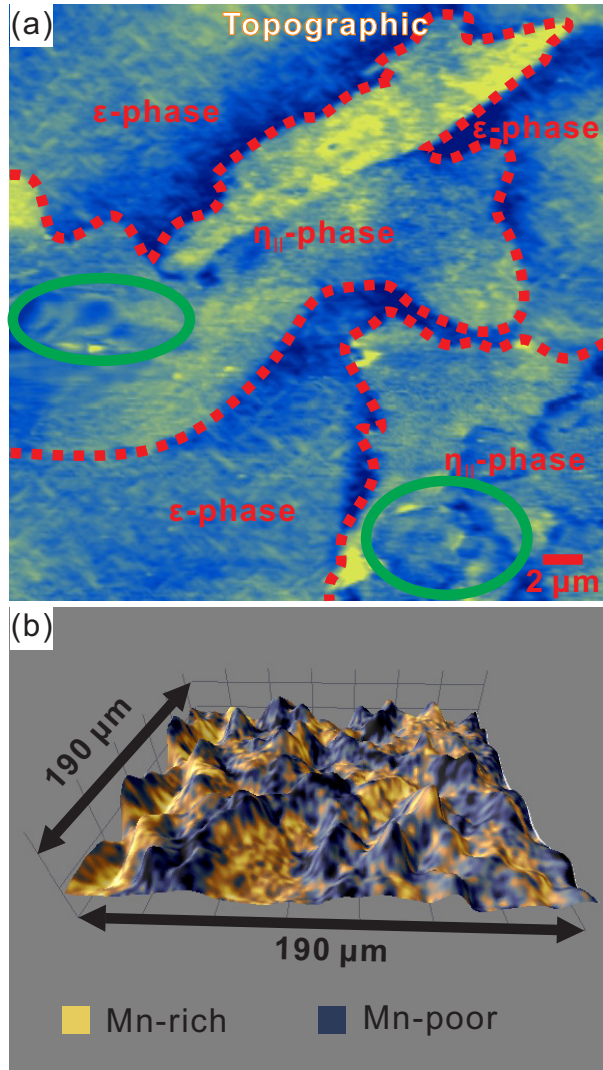


Figure 5: Microscopy data of the mixed phase sample. (a) Larger scale AFM image showing adjacent domains of the two phases (d) A 3D SEM topographic image overlaid with a heat map of Mn concentration

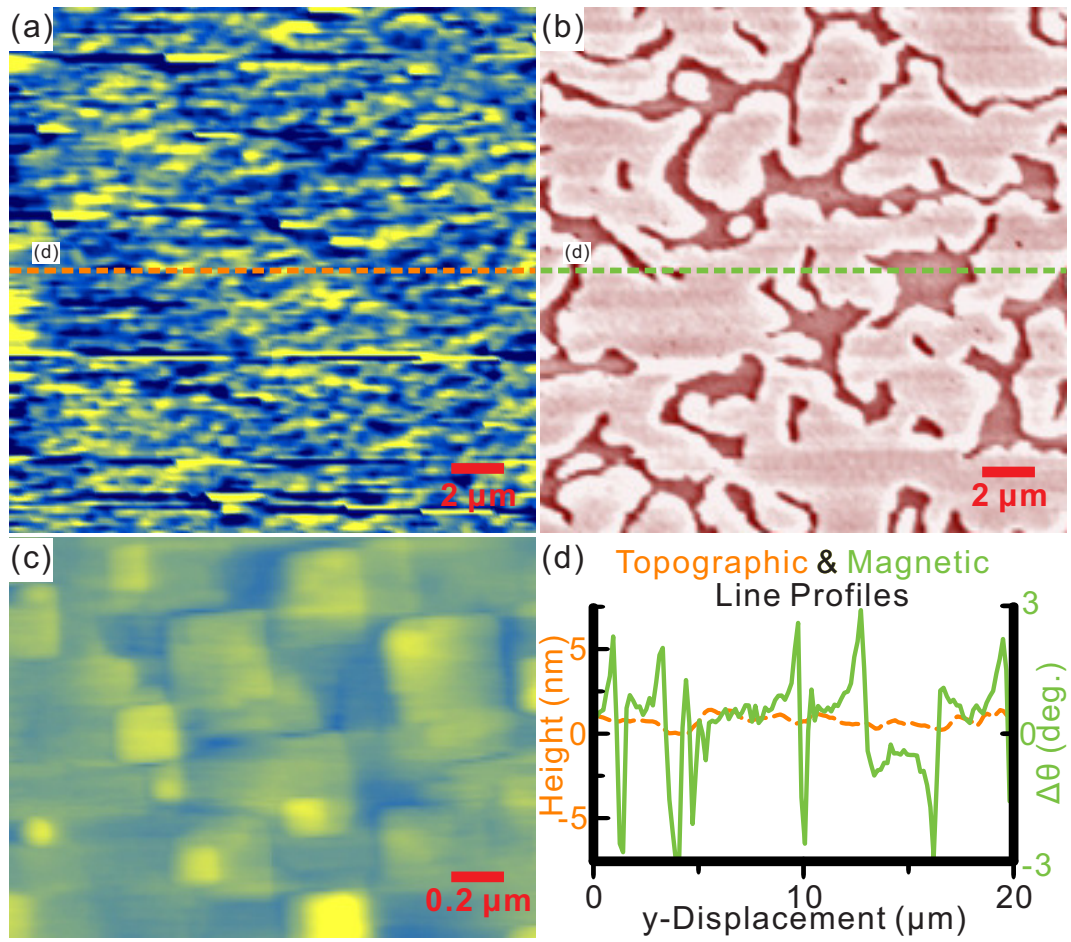


Figure 6: (a) Larger scale AFM image of epsilon surface (b) MFM image over the same area shown in a) (c) Smaller scale AFM image of the epsilon surface (d) Topographic and magnetic line profiles shown in a) and b)

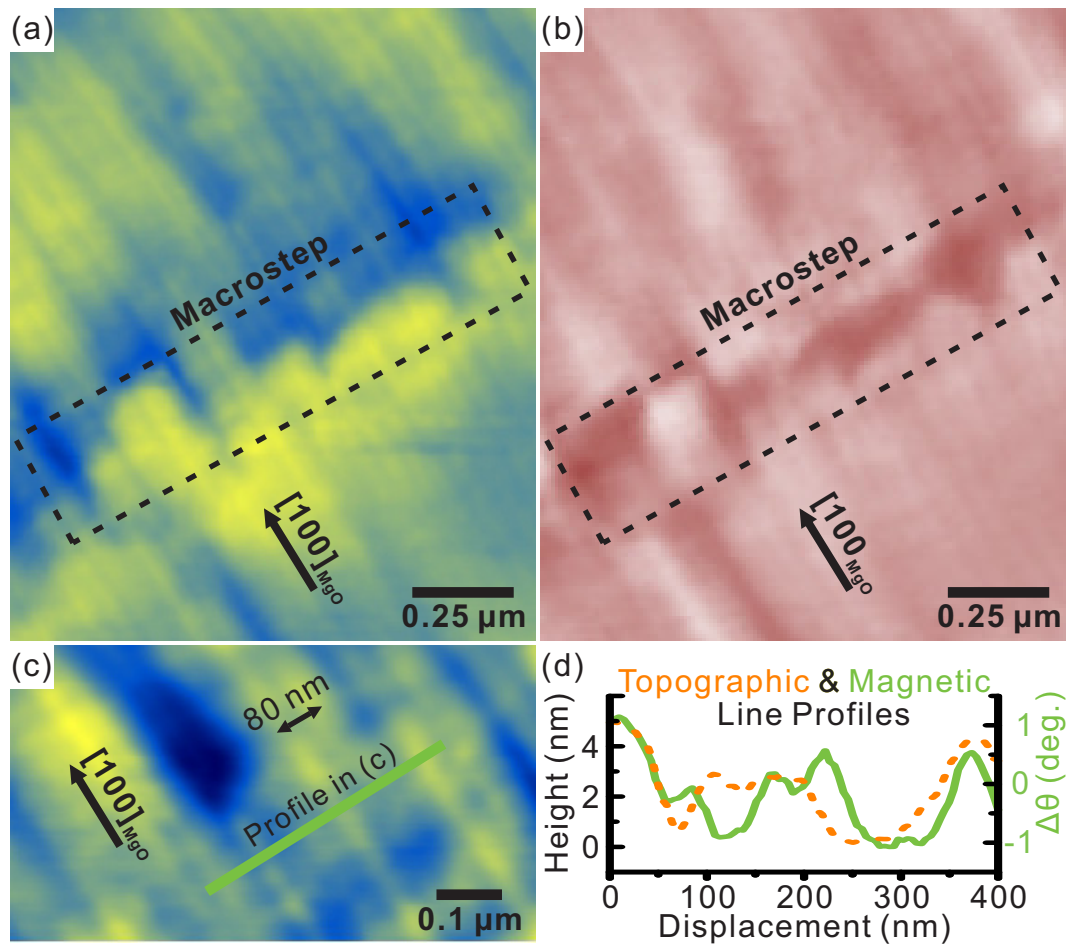


Figure 7: (a) AFM image of  $\zeta$ -phase surface (b) MFM image over the same area shown in a) (c) Zoom-in of region from a) (d) Topographic line profile across line shown in b) and corresponding magnetic line profile

Growth plane (h k l)	Observed (Å) XRD	Expected (Å) out-of-plane	Observed (Å) RHEED	Expected (Å) in-plane
<b><math>\varepsilon</math>-phase</b>				
(0 0 2)	3.86±0.01	3.86	3.88±0.01	3.86
<b>Mixed phase (<math>\eta</math>-phase &amp; <math>\varepsilon</math>-phase)</b>				
$\eta$ -(0 2 0)	obscured by 4.213 MgO peak	4.21		4.04/4.21 or 4.13 avg.
$\varepsilon$ -(0 0 2)	3.87±0.01	3.86		3.86
Average of $\eta$ -(0 2 0) & $\varepsilon$ -(0 0 2)			3.97±0.02	3.99
<b><math>\gamma</math>-type <math>\zeta</math>-phase</b>				
(1 0 1)	2.15±0.01	2.16	5.23±0.15	5.36
(3 0 4)*			3.80±0.24	3.99
(0 0 2)	4.53±0.01	4.55	4.95±0.10	4.91
(1 0 0)	2.43±0.01	2.45	5.23±0.15	5.36
*This plane is 7.79° off (101) and associated with a facet, which would be formed at the surface between Mn atoms in nearest (101) Mn-planes of different bases.				

Table 1: Comparisons between XRD and RHEED data and the values expected from the data. All RHEED measurements were taken along the MgO[100] direction.